Wafer-scale mapping of carrier density and mobility with terahertz time-domain ellipsometry

VERDAD C. AGULTO,[1] TOSHIYUKI IWAMOTO,[1,2] ZIXI ZHAO,[1] SHUANG LIU,[1] KOSAKU KATO,[1] AND MAKOTO NAKAJIMA[1,*]

[1]*Institute of Laser Engineering, Osaka University, 2-6 Yamadaoka, Suita, Osaka 565-0871, Japan*
[2]*Nippo Precision Co., Ltd., 734 Hosaka, Nirasaki, Yamanashi 407-0175, Japan*
**nakajima.makoto.ile@osaka-u.ac.jp*

Received XX Month XXXX; revised XX Month, XXXX; accepted XX Month XXXX; posted XX Month XXXX (Doc. ID XXXXX); published XX Month XXXX

Terahertz (THz) measurements are increasingly valued for nondestructive testing of materials in power devices and other applications. Hence, there is a growing demand for highly accurate characterization methods in the THz range. Here we demonstrate the application of THz time-domain ellipsometry (THz-TDE) to large-scale, quantitative mapping of semiconductor wafers. While THz-TDE is an established technique, its application in wafer-scale mapping, which is an important process in the semiconductor industry, has not yet been demonstrated. In this work, we highlight the effectiveness of THz-TDE by mapping the electrical properties of a widely used semiconductor, silicon carbide (SiC). Spatial distribution maps of conductivity, carrier density, and mobility of a commercial 4-inch SiC wafer are derived using the measured ellipsometric parameters. THz-TDE mapping offers a nondestructive, contactless testing method to evaluate semiconductor quality and electrical homogeneity and is notably suitable for doped semiconductors characterized by high THz absorption.

Carrier density and mobility are important properties that significantly influence the performance of semiconductor devices. Thus, it is essential to measure these properties and evaluate their spatial distribution in semiconductor wafers for production monitoring and process control. Silicon carbide (SiC) has become a backbone of today's semiconductor industry, serving as a base material for metal-oxide-semiconductor field-effect transistors and Schottky diodes. SiC is being adopted across diverse applications, including power electronic devices, electric vehicles, energy storage systems, and solar inverters. As the semiconductor industry experiences unprecedented growth, the demand for high-quality SiC wafers and advanced characterization tools is also increasing rapidly.

The four-point probe (4PP) method is a widely used resistivity mapping technique for testing semiconductors and thin films. However, this method may induce mechanical damage to the sample under test due to excessive needle loading or electrical damage due to excessive currents [1]. Mercury capacitance-voltage (C-V) profiling is also used by the semiconductor industry for epitaxial wafers. Although it has a high measurement repeatability [2], safety issues concerning the mercury probe and the possible contamination of the wafer or the measurement platform cannot be neglected. To mitigate the risk of damage to pristine wafer surfaces and delicate thin films and epilayers, the use of contactless mapping methods is becoming increasingly important.

Various contactless methods for conductivity and sheet resistance measurements commonly used in the semiconductor industry have been extensively reviewed, which include capacitive resistivity mapping technique for high-resistivity semiconductors, eddy current measurements, microwave-based techniques, and non-contact C-V profiling via corona-Kelvin metrology which does not use mercury probes [1–5]. Additionally, free-carrier absorption occurring in the infrared (IR) and terahertz (THz) regions can be leveraged to determine the carrier density and mobility of semiconductors [6]. Large-scale semiconductor mapping has been demonstrated using IR reflectance spectroscopy [7,8], as well as nanoscale local conductivity mapping with recent IR and THz scattering-type scanning near-field optical microscopy (s-SNOM) technologies [9,10]. Furthermore, one emerging application of THz time-domain spectroscopy (THz-TDS) that is slowly gaining interest is the quantitative mapping of graphene and other substrates [11–15].

Terahertz waves have emerged as a powerful tool in both fundamental and applied sciences, spanning disciplines such as spintronics [16–18], ultrafast beam diagnostics [19], and materials characterization [20–23], among others. For industrial applications, there is a growing demand for highly accurate characterization methods and measurement tools in the THz range [11]. THz-TDS is a well-established technique to characterize the dielectric properties of materials in the THz region, typically employing a transmission configuration, rather than reflection, for higher phase accuracy. However, transmission measurements pose difficulties with optically thick and highly absorbing materials such as doped semiconductors. Additionally, in THz-TDS measurements, the sample thickness is a crucial parameter. Hence, thickness variation must be carefully considered in mapping measurements of wafers and substrates [13–15], as thickness variation of a substrate within a few microns can result in time delay of the THz pulse of up to tens of femtoseconds and lead to large phase shifts. These challenges are addressed by THz time-domain ellipsometry (THz-TDE) [24,25].

THz-TDE combines the foundations of THz-TDS and ellipsometry techniques [26]. In ellipsometry, the measured values (Ψ, Δ) are defined from the ratio of the complex amplitude reflection coefficients for p and s polarizations [27]:

$$\tilde{\rho} \equiv \tan\Psi \exp i\Delta \equiv \frac{\tilde{r}_p}{\tilde{r}_s} \equiv \left(\frac{\tilde{E}_{r,p}}{\tilde{E}_{i,p}}\right) \Big/ \left(\frac{\tilde{E}_{r,s}}{\tilde{E}_{i,s}}\right) !\, ! \qquad (1)$$

where $\tilde{E}$ denotes the complex-valued electric field and the subscripts r and i represent reflected and incident fields, respectively. The incident field is linearly polarized with equal p and s components, i.e., $\tilde{E}_{i,p} = \tilde{E}_{i,s}$. Investigations of wide-bandgap semiconductors such as GaN, ZnO, and β-Ga_2O_3 using both time-domain and continuous-wave THz ellipsometry techniques have been previously conducted [24,25,28,29]. The main advantages of THz-TDE are: (1) it allows for the characterization of optically thick and highly absorbing samples such as doped semiconductors with its reflection configuration; (2) it is a reference-free method (ellipsometry), thus the problem of phase inaccuracy in reflection THz-TDS is eliminated; and (3) it has a coherent detection (THz-TDS) scheme, thus both amplitude and phase information can be measured. Furthermore, the substrate thickness is not a prerequisite parameter as only the surface reflection is sufficiently considered, provided that any multiple reflection within the substrate can be truncated from the main surface reflection. In this work, we demonstrate wafer-scale mapping of n-type SiC electrical properties using THz-TDE. The wafer has a 4-inch diameter and a thickness of 350 μm.

In the THz-TDE measurements, the time traces of p and s polarizations reflected off a sample, denoted as $E_{r,p}(t)$ and $E_{r,s}(t)$, are initially recorded. Subsequently, Fourier transformations of these time traces yield the amplitude and phase information in the frequency domain, which are then used to acquire the amplitude ratio, expressed as $\tan\Psi(\omega) = |\tilde{E}_{r,p}(\omega)| / |\tilde{E}_{r,s}(\omega)|$, and the phase (δ) difference, $\Delta(\omega) = \delta_{r,p}(\omega) - \delta_{r,s}(\omega)$. These so-called ellipsometric parameters are related to the optical constants of the material, which hold information about its carrier transport properties and can be analyzed to extract the carrier density, scattering time, mobility, and conductivity through suitable optical conductivity models.

Here we demonstrate THz-TDE mapping using the THz time-domain ellipsometer, Tera Evaluator (Nippo Precision, Co., Ltd.). The ellipsometer employs photoconductive dipole antennas for both THz generation and detection and utilizes femtosecond laser excitation with a central wavelength of approximately 800 nm and a pulse width less than 120 fs. The angle of incidence θ_0 is approximately 70° which is close to the Brewster's angle of semiconductors, and the size of the THz focal spot is approximately 4 mm (short axis diameter) by 10 mm (long axis diameter). Here the long axis is parallel to the plane of incidence. The polarizers utilized in the ellipsometric measurements have an excellent extinction ratio of 10^5:1, and the temporal accuracy for the measured p- and s-polarized THz pulses is ensured through the use of a rotating analyzer, the detailed data processing of which is described elsewhere [24], thereby guaranteeing high precision in the measured amplitude and phase. The measurement frequency range is 1.0 to 3.0 THz. To implement the mapping measurement, a motorized r-theta stage was used for the automatic translation of the wafer. The wafer was translated in the radial direction, which is parallel to the short axis of the THz focal spot, and rotated in the theta direction such that the measurement points were evenly spaced at 2-mm intervals in both the x and y directions of the sample plane. This 2-mm spacing corresponds approximately to the full-width-at-half-maximum (FWHM) of the THz beam along the radial direction where the sample is translated, representing the maximum achievable spatial resolution. Sample stage height adjustment and tilt correction were implemented automatically at each mapping point to ensure the local surface is at the focal point and perpendicular to the normal axis, preventing measurement errors due to possible thickness variations across the wafer. The maximum measurement time at a single point, including sample height adjustment and tilt correction, is approximately 90 seconds when using the highest frequency resolution and measurement accuracy.

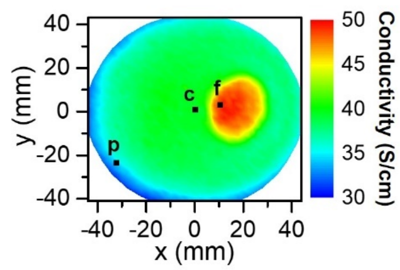

Fig. 1. DC conductivity map of n-type 4H-SiC wafer derived from THz-TDE measurement. The three indicated points represent distinct areas on the wafer: **f** – facet, **c** – center, **p** – periphery.

Figure 1 shows the DC conductivity map obtained from THz-TDE measurements of a commercial 4-inch, nitrogen-doped 4H-SiC wafer (TankeBlue Semiconductor Co., Ltd.), with a surface orientation of 4° off-axis from the <0001> direction. Higher conductivities were observed in the middle of the wafer, which corresponds to the inherent {0001} growth facet of SiC as will be elaborated on later, and the conductivity tends to decrease towards the periphery of the wafer. The DC conductivity (σ_{DC}) was determined using the equation $\sigma_{DC} = Ne\mu$ where e is electron charge and N and μ are carrier density and mobility obtained from point-by-point best-fit curve analysis of ellipsometric parameters measured by THz-TDE as will be discussed below. The average resistivity of the wafer is 0.026 ± 0.004 Ω·cm, which is in close agreement with the wafer specification, 0.015−0.028 Ω·cm.

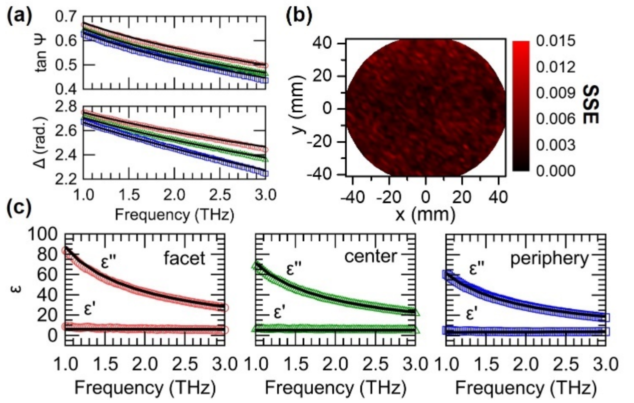

Fig. 2. (a) Ellipsometric parameters measured at different areas on the n-type 4H-SiC wafer, (b) spatial distribution of the sum of squared errors (SSE) from the ellipsometric parameter fitting, and (c) the corresponding complex dielectric function, $\tilde{\varepsilon} = \varepsilon' - i\varepsilon''$, obtained for each area.

Figure 2(a) shows the spectra of ellipsometric parameters measured at distinct locations on the SiC wafer: within the facet region (red), at the center (green), and around the periphery (blue), as indicated by points **f**, **c**, and **p**, respectively, in Fig. 1. These spots signify varying conductivity properties, with the facet area showing high conductivity, the periphery exhibiting low conductivity, and the center falling in between. The carrier density N and mobility μ values at each mapping point were determined by performing a least-squares fit of the ellipsometric parameters using Eq. (2), which was derived by substituting $\tilde{r}_p$ and $\tilde{r}_s$ in Eq. (1) with the corresponding Fresnel equations for light reflection at an air/sample interface:

$$\tan\Psi \exp i\Delta = \left(\frac{\tilde{n}_1\cos\theta_0 - \tilde{n}_0\cos\theta_1}{\tilde{n}_1\cos\theta_0 + \tilde{n}_0\cos\theta_1}\right) \Big/ \left(\frac{\tilde{n}_0\cos\theta_0 - \tilde{n}_1\cos\theta_1}{\tilde{n}_0\cos\theta_0 + \tilde{n}_1\cos\theta_1}\right). \quad (2)$$

Here, $\tilde{n}_0$ and $\tilde{n}_1$ are the complex refractive indices of air ($\tilde{n}_0 = 1 - i0$) and sample, respectively, while θ_1 can be calculated from the angle of incidence θ_0 using Snell's law. In the fitting, the Drude equation was used to model the optical constants of SiC in the THz region [30]. The Drude model is expressed by

$$\tilde{\varepsilon} = \tilde{n}^2 = \varepsilon_{bg}\left(1 - \frac{\omega_p^2}{\omega^2 - i\omega\gamma}\right) \quad (3)$$

where ω is angular frequency. The plasma frequency ω_p and the carrier scattering rate γ, which is the inverse of the scattering time τ, are defined by $\omega_p = \left(e^2N/\varepsilon_0\varepsilon_{bg}m^*\right)^{1/2}$ and $\gamma = 1/\tau = e/m^*\mu$, where ε_0 is the permittivity of free space. The background dielectric constant ε_{bg} and the electron effective mass m^* for SiC were taken to be 9.8, as measured from a semi-insulating SiC using THz-TDS, and $0.30m_e$ (where m_e is the electron mass), respectively [31]. Figure 2(b) illustrates the quality of fit, indicated by the sum of squared errors (SSE). The uniform distribution of low SSE values underscores the accuracy of the retrieved free-carrier parameters across the different parts of the wafer.

It is important to note that the optical constants used in the ellipsometry analysis are regarded as pseudo-dielectric function [27]. The pseudo-dielectric function represents the dielectric function assuming an isotropic material with a perfectly flat surface and with no surface overlayer of any type. Nevertheless, the pseudo-dielectric function can also be applied to uniaxial materials such as SiC in special cases where the cross-polarization reflection coefficients are zero [32]. One such case is when the optic axis of the uniaxial sample is oriented normal to the sample surface. With this specific configuration, the pseudo-dielectric function approximates the dielectric function perpendicular to the optic axis [32]. In the case of our SiC sample, the optic axis is 4° off from the surface normal. This off angle is very small and can thus be ignored in the approximation [33]. The pseudo-dielectric function is calculated directly from the measured ellipsometric parameters using the following equation [27]:

$$\tilde{\varepsilon} = \tilde{n}_0^2\sin^2\theta_0\left[1 + \tan^2\theta_0\left(\frac{1-\tilde{\rho}}{1+\tilde{\rho}}\right)^2\right] \quad (4)$$

where $\tilde{n}_0$ is the complex refractive index of air ($\tilde{n}_0 = 1 - i0$) and θ_0 is the angle of incidence. Using Eq. (4), the dielectric function of the SiC wafer, $\tilde{\varepsilon} = \varepsilon' - i\varepsilon''$, was obtained as shown in Fig. 2(c). The facet region demonstrates higher ε'' compared to the other areas, indicating increased loss attributed to free-carrier absorption, consistent with the facet's high conductivity. Conversely, the periphery, characterized by lower conductivity, exhibits lower ε''. The equivalent Drude fitting is also shown for the dielectric function. Clearly, the optical constants of SiC obtained by THz-TDE are well-described by the Drude model.

Figures 3(a) and 3(b) show the spatial maps of the carrier density and mobility of the SiC wafer, respectively. The area in the middle of the wafer that is characterized by a higher carrier density, shown in Fig. 3(a), corresponds to the {0001} growth facet that appears near the center of the crystal boule during sublimation growth of SiC [34,35]. On the other hand, the lowest carrier density is observed at the periphery of the wafer. This radial distribution of the conductivity, i.e., higher carrier densities in the middle and lower carrier densities at the periphery, can be explained by the growth process of SiC [34,36]. The fast spiral growth on the {0001} facet enhances the dopant incorporation in the facet region, resulting in a higher carrier density. Conversely, the dopant density diminishes toward the outer region of the wafer. This phenomenon is common in commercial n-type 4H-SiC wafers [37]. Furthermore, higher carrier densities lead to increased carrier scattering, which reduces mobility. Thus, the facet area exhibits lower mobilities compared to the rest of the wafer, as shown in Fig. 3(b). Figures 3(c) and 3(d) show the spatial profiles of the carrier density and mobility along the horizontal dashed lines in Fig. 3(a) and Fig. 3(b). The facet region demonstrates notably higher carrier densities and lower mobilities. The data points represent an average of three separate measurements, demonstrating the satisfactory repeatability of the mapping measurements, with a standard deviation of less than 5% for the carrier density and mobility. For the conductivity values, the standard deviation was even lower at less than 1%. As for the average values in each region of the wafer, the average carrier densities within the facet, the larger area surrounding the facet, and the wafer's periphery are (6.2 ± 1.3), (3.6 ± 0.7), and (2.8 ± 0.3) × 10^{18} cm^{-3}, respectively, with 95% confidence interval. Corresponding average mobilities are 47.3 ± 8.2, 65.4 ± 8.3, and 75.6 ± 6.4 cm^2 V^{-1} s^{-1}, while the average conductivities are 47 ± 12, 38 ± 9, and 34 ± 5 S cm^{-1}, respectively.

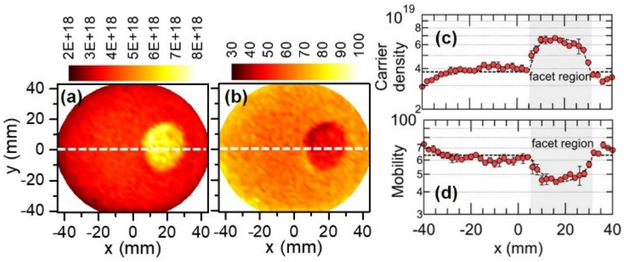

Fig. 3. (a,b) Spatial distributions of the carrier density (cm^{-3}) and mobility ($cm^2V^{-1}s^{-1}$) of n-type 4H-SiC wafer obtained by THz-TDE mapping. (c,d) Carrier density and mobility profiles along the horizontal dashed lines in (a,b). Results of three measurements are averaged. The dashed lines serve as guide to eye.

In summary, we demonstrated the effectiveness of THz-TDE in large-scale, quantitative mapping of semiconductors by measuring the spatial distribution of the carrier transport properties of a commercial SiC wafer. THz-TDE mapping revealed the growth facet region characterized by a higher conductivity, consistent with the inherent characteristic of SiC wafers. In contrast to other contactless resistivity mapping methods, THz-TDE offers the capability to determine not just the resistivity or conductivity but also the carrier density and mobility. These quantities provide deeper insights into the uniformity and quality of the semiconductor wafer in the interest of device performance. The range of carrier densities that can be evaluated spans widely, from 10^{16}–10^{21} cm^{-3} [25]. With its contactless approach, THz-TDE is advantageous for pristine wafer characterization and beneficial for increasing production yield. Bulk substrates with thicknesses exceeding $5d_p$, where d_p is penetration depth of THz waves, can be analyzed in a manner presented in this study. Furthermore, owing to the reference-free characteristic of THz-TDE and the implementation of the reflection modality, errors in parameter extraction that may arise from wafer thickness variation can be prevented systematically. We anticipate that THz-TDE could be a useful nondestructive testing tool for production monitoring and failure analysis in the semiconductor industry.

Funding. This work was supported by METI Monozukuri R&D Support Grant Program for SMEs Grant Number JPJ005698, partly supported by JKA and its promotion funds from AUTORACE, and partly supported by JSPS KAKENHI Grant Numbers JP24H00317, JP23K17748, JP24H02232.

Disclosures. The authors declare no conflicts of interest.

Data Availability. Data underlying the results presented in this paper are not publicly available at this time but may be obtained from the authors upon reasonable request.

References

1. J. Krupka, Meas Sci Technol **24**, 062001 (2013).
2. J. Mizsei and A. Czett, Appl Surf Sci **301**, 19–23 (2014).
3. R. Stibal, S. Müller, W. Jantz, *et al.*, Phys Stat Sol (c) **0**(3), 1013–1018 (2003).
4. D. Nguyen, K. Hogan, A. Blew, *et al.*, J Cryst Growth **272**, 59–64 (2004).
5. A. Savtchouk, M. Wilson, D. Marinskiy, *et al.*, Materials Science Forum **1089**, 51–56 (2023).
6. D. Grischkowsky, S. Keiding, M. v. Exter, *et al.*, J Opt Soc Am B **7**(10), 2006–2015 (1990).
7. K. Narita, Y. Hijikata, H. Yaguchi, *et al.*, Jpn J Appl Phys **43**(8A), 5151–5156 (2004).
8. S. Oishi, Y. Hijikata, H. Yaguchi, *et al.*, Jpn J Appl Phys **45**(46), L1226–L1229 (2006).
9. E.T. Ritchie, C.B. Casper, T.A. Lee, *et al.*, J Phys Chem C, **126**, 4515–4521 (2022).
10. T.L. Cocker, V. Jelic, R. Hillenbrand, *et al.*, Nat Photonics **15**, 558–569 (2021).
11. A. Leitenstorfer, A.S. Moskalenko, T. Kampfrath, *et al.*, J Phys D: Appl Phys **56**, 223001 (2023).
12. J.D. Buron, D.H. Petersen, P. Bøggild, *et al.*, Nano Lett **12**, 5074–5081 (2012).
13. J. Hennig, J. Klier, S. Duran, *et al.*, Opt Express **32**(12), 21028–21041 (2024).
14. K. Muthuramalingam and W.-C. Wang, Mater Sci Semicond Process **170**, 107932 (2024).
15. M. Herrmann, M. Tani, K. Sakai, *et al.*, J Appl Phys **91**(3), 1247–1250 (2002).
16. M.A. Weiss, A. Herbst, J. Schlegel, *et al.*, Nat Commun **14**, 7651 (2023).
17. G. Fitzky, M. Nakajima, Y. Koike, *et al.*, Phys Rev Lett **127**(10), 107401 (2021).
18. Z. Zhang, M. Kanega, K. Maruyama, *et al.*, Nat Mater (2024). https://doi.org/10.1038/s41563-024-02034-4
19. M. Ota, K. Kan, S. Komada, *et al.*, Nat Phys **18**, 1436–1440 (2022).
20. V.C. Agulto, K. Toya, T.N.K. Phan, *et al.*, Appl Phys Lett **118**, 042101 (2021).
21. V.C. Agulto, Z. Ling, Z. Zhao, *et al.*, Opt Lett **48**(23), 6324–6327 (2023).
22. J. Wang, W. Cai, W. Lu, *et al.*, Nature **631**, 67–72 (2024).
23. K. Makino, K. Kato, Y. Saito, *et al.*, J Mater Chem C Mater **7**, 8209–8215 (2019).
24. V.C. Agulto, T. Iwamoto, H. Kitahara, *et al.*, Sci Rep **11**, 18129 (2021).
25. T. Iwamoto, V.C. Agulto, S. Liu, *et al.*, Jpn J Appl Phys **62**, SF1011 (2023).
26. T. Nagashima and M. Hangyo, Appl Phys Lett **79**(24), 3917–3919 (2001).
27. H. Fujiwara, *Spectroscopic Ellipsometry: Principles and Applications* (John Wiley & Sons, Chichester, 2007).
28. Z. Zhao, V.C. Agulto, T. Iwamoto, *et al.*, Opt Matter: X **24**, 100352 (2024).
29. P. Gopalan, S. Knight, A. Chanana, *et al.*, Appl Phys Lett **117**, 252103 (2020).
30. A. Rubano, M. Wolf, and T. Kampfrath, Appl Phys Lett **105**, 032104 (2014).
31. H. Harima, S. Nakashima, and T. Uemura, J Appl Phys **78**(3), 1996–2005 (1995).
32. G.E. Jellison, Jr. and J.S. Baba, J Opt Soc Am A **23**(2), 468–475 (2006).
33. D.E. Aspnes, J Opt Soc Am **70**(10), 1275–1277 (1980).
34. T. Kimoto and J.A. Cooper, *Fundamentals of Silicon Carbide Technology: Growth, Characterization, Devices and Applications* (John Wiley & Sons, Singapore, 2014).
35. Q. Li, A.Y. Polyakov, M. Skowronski, *et al.*, J Appl Phys **97**, 113705 (2005).
36. J.Y. Yu, X.L. Yang, Y. Peng, *et al.*, Crystallogr Rep **65**(7), 1231–1236 (2020).
37. L. Zhao and H. Wu, J Cryst Growth **507**, 109–112 (2019).

References

1. J. Krupka, "Contactless methods of conductivity and sheet resistance measurement for semiconductors, conductors and superconductors," Meas Sci Technol **24**, 062001 (2013).
2. J. Mizsei and A. Czett, "Characterization of 4H-SiC surfaces by non-destructive techniques based on capacitance voltage measurements," Appl Surf Sci **301**, 19–23 (2014).
3. R. Stibal, S. Müller, W. Jantz, G. Pozina, B. Magnusson, and A. Ellison, "Nondestructive topographic resistivity evaluation of semi-insulating SiC substrates," Phys Stat Sol (c) **0**(3), 1013–1018 (2003).
4. D. Nguyen, K. Hogan, A. Blew, and M. Cordes, "Improved process control, lowered costs and reduced risks through the use of non-destructive mobility and sheet carrier density measurements on GaAs and GaN wafers," J Cryst Growth **272**, 59–64 (2004).
5. A. Savtchouk, M. Wilson, D. Marinskiy, B. Schrayer, C. Almeida, and J. Lagowski, "Recent Progress in Non-Contact Electrical Characterization for SiC and Related Compounds," Materials Science Forum **1089**, 51–56 (2023).
6. D. Grischkowsky, S. Keiding, M. v. Exter, and Ch. Fattinger, "Far-infrared time-domain spectroscopy with terahertz beams of dielectrics and semiconductors," J Opt Soc Am B **7**(10), 2006–2015 (1990).
7. K. Narita, Y. Hijikata, H. Yaguchi, S. Yoshida, and S. Nakashima, "Characterization of Carrier Concentration and Mobility in n-type SiC Wafers Using Infrared Reflectance Spectroscopy," Jpn J Appl Phys **43**(8A), 5151–5156 (2004).
8. S. Oishi, Y. Hijikata, H. Yaguchi, and S. Yoshida, "Simultaneous Determination of Carrier Concentration, Mobility, and Thickness of SiC Homoepilayers by Infrared Reflectance Spectroscopy," Jpn J Appl Phys **45**(46), L1226–L1229 (2006).
9. E.T. Ritchie, C.B. Casper, T.A. Lee, and J.M. Atkin, "Quantitative Local Conductivity Imaging of Semiconductors Using Near-Field Optical Microscopy," J Phys Chem C, **126**, 4515–4521 (2022).
10. T.L. Cocker, V. Jelic, R. Hillenbrand, and F.A. Hegmann, "Nanoscale terahertz scanning probe microscopy," Nat Photonics **15**, 558–569 (2021).
11. A. Leitenstorfer, A.S. Moskalenko, T. Kampfrath, J. Kono, E. Castro-Camus, K. Peng, N. Qureshi, D. Turchinovich, K. Tanaka, A.G. Markelz, M. Havenith, C. Hough, H.J. Joyce, W.J. Padilla, B. Zhou, K.-Y. Kim, X.-C. Zhang, P.U. Jepsen, S. Dhillon, M. Vitiello, E. Linfield, A.G. Davies, M.C. Hoffmann, R. Lewis, M. Tonouchi, P. Klarskov, T.S. Seifert, Y.A. Gerasimenko, D. Mihailovic, R. Huber, J.L. Boland, O. Mitrofanov, P. Dean, B.N. Ellison, P.G. Huggard, S.P. Rea, C. Walker, D.T. Leisawitz, J.R. Gao, C. Li, Q. Chen, G. Valušis, V.P. Wallace, E. Pickwell-MacPherson, X. Shang, J. Hesler, N. Ridler, C.C. Renaud, I. Kallfass, T. Nagatsuma, J.A. Zeitler, D. Arnone, M.B. Johnston, and J. Cunningham, "The 2023 terahertz science and technology roadmap," J Phys D: Appl Phys **56**, 223001 (2023).
12. J.D. Buron, D.H. Petersen, P. Bøggild, D.G. Cooke, M. Hilke, J. Sun, E. Whiteway, P.F. Nielsen, O. Hansen, A. Yurgens, and P.U. Jepsen, "Graphene Conductance Uniformity Mapping," Nano Lett **12**, 5074–5081 (2012).
13. J. Hennig, J. Klier, S. Duran, K.-S. Hsu, J. Beyer, C. Röder, F.C. Beyer, N. Schüler, N. Vieweg, K. Dutzi, G. von Freymann, and D. Molter, "Wide-range resistivity characterization of semiconductors with terahertz time-domain spectroscopy," Opt Express **32**(12), 21028–21041 (2024).
14. K. Muthuramalingam and W.-C. Wang, "Non-destructive mapping of electrical properties of semi-insulating compound semiconductor wafers using terahertz time-domain spectroscopy," Mater Sci Semicond Process **170**, 107932 (2024).
15. M. Herrmann, M. Tani, K. Sakai, and R. Fukasawa, "Terahertz imaging of silicon wafers," J Appl Phys **91**(3), 1247–1250 (2002).
16. M.A. Weiss, A. Herbst, J. Schlegel, T. Dannegger, M. Evers, A. Donges, M. Nakajima, A. Leitenstorfer, S.T.B. Goennenwein, U. Nowak, and T. Kurihara, "Discovery of ultrafast spontaneous spin switching in an antiferromagnet by femtosecond noise correlation spectroscopy," Nat Commun **14**, 7651 (2023).
17. G. Fitzky, M. Nakajima, Y. Koike, A. Leitenstorfer, and T. Kurihara, "Ultrafast Control of Magnetic Anisotropy by Resonant Excitation of $4f$ Electrons and Phonons in $Sm_{0.7}Er_{0.3}FeO_3$," Phys Rev Lett **127**(10), 107401 (2021).
18. Z. Zhang, M. Kanega, K. Maruyama, T. Kurihara, M. Nakajima, T. Tachizaki, M. Sato, Y. Kanemitsu, and H. Hirori, "Spin switching in $Sm_{0.7}Er_{0.3}FeO_3$ triggered by terahertz magnetic-field pulses," Nat Mater (2024). https://doi.org/10.1038/s41563-024-02034-4
19. M. Ota, K. Kan, S. Komada, Y. Wang, V.C. Agulto, V.K. Mag-usara, Y. Arikawa, M.R. Asakawa, Y. Sakawa, T. Matsui, and M. Nakajima, "Ultrafast visualization of an electric field under the Lorentz transformation," Nat Phys **18**, 1436–1440 (2022).
20. V.C. Agulto, K. Toya, T.N.K. Phan, V.K. Mag-usara, J. Li, M.J.F. Empizo, T. Iwamoto, K. Goto, H. Murakami, Y. Kumagai, N. Sarukura, M. Yoshimura, and M. Nakajima, "Anisotropic complex refractive index of β-Ga_2O_3 bulk and epilayer evaluated by terahertz time-domain spectroscopy," Appl Phys Lett **118**, 042101 (2021).
21. V.C. Agulto, Z. Ling, Z. Zhao, S. Feng, K. Kato, M. Haga, V.K. Mag-usara, M. Yoshimura, and M. Nakajima, "Design and fabrication of a microcoil metamaterial absorber for the sub-terahertz region," Opt Lett **48**(23), 6324–6327 (2023).
22. J. Wang, W. Cai, W. Lu, S. Lu, E. Kano, V.C. Agulto, B. Sarkar, H. Watanabe, N. Ikarashi, T. Iwamoto, M. Nakajima, Y. Honda, and H. Amano, "Observation of 2D-magnesium-intercalated gallium nitride superlattices," Nature **631**, 67–72 (2024).
23. K. Makino, K. Kato, Y. Saito, P. Fons, A. V. Kolobov, J. Tominaga, T. Nakano, and M. Nakajima, "Terahertz spectroscopic characterization of $Ge_2Sb_2Te_5$ phase change materials for photonics applications," J Mater Chem C Mater **7**, 8209–8215 (2019).
24. V.C. Agulto, T. Iwamoto, H. Kitahara, K. Toya, V.K. Mag-usara, M. Imanishi, Y. Mori, M. Yoshimura, and M. Nakajima, "Terahertz time-domain ellipsometry with high precision for the evaluation of GaN crystals with carrier densities up to 10^{20} cm^{-3}," Sci Rep **11**, 18129 (2021).
25. T. Iwamoto, V.C. Agulto, S. Liu, Y. Wang, V.K. Mag-usara, T. Fujii, K. Goto, Y. Kumagai, and M. Nakajima, "Characterization of electrical properties of β-Ga_2O_3 epilayer and bulk GaAs using terahertz time-domain ellipsometry," Jpn J Appl Phys **62**, SF1011 (2023).
26. T. Nagashima and M. Hangyo, "Measurement of complex optical constants of a highly doped Si wafer using terahertz ellipsometry," Appl Phys Lett **79**(24), 3917–3919 (2001).
27. H. Fujiwara, *Spectroscopic Ellipsometry: Principles and Applications* (John Wiley & Sons, Chichester, 2007).
28. Z. Zhao, V.C. Agulto, T. Iwamoto, K. Kato, K. Yamanoi, T. Shimizu, N. Sarukura, T. Fujii, T. Fukuda, M. Yoshimura, and M. Nakajima, "Investigation of the optical and electrical properties of zinc oxide by terahertz time domain ellipsometry," Opt Matter: X **24**, 100352 (2024).
29. P. Gopalan, S. Knight, A. Chanana, M. Stokey, P. Ranga, M.A. Scarpulla, S. Krishnamoorthy, V. Darakchieva, Z. Galazka, K. Irmscher, A. Fiedler, S. Blair, M. Schubert, and B. Sensale-Rodriguez, "The anisotropic quasi-static permittivity of single-crystal β-Ga_2O_3 measured by terahertz spectroscopy," Appl Phys Lett **117**, 252103 (2020).
30. A. Rubano, M. Wolf, and T. Kampfrath, "Terahertz conductivity and ultrafast dynamics of photoinduced charge carriers in intrinsic 3C and 6H silicon carbide," Appl Phys Lett **105**, 032104 (2014).
31. H. Harima, S. Nakashima, and T. Uemura, "Raman scattering from anisotropic LO-phonon–plasmon–coupled mode in *n*-type 4H– and 6H–SiC," J Appl Phys **78**(3), 1996–2005 (1995).
32. G.E. Jellison, Jr. and J.S. Baba, "Pseudodielectric functions of uniaxial materials in certain symmetry directions," J Opt Soc Am A **23**(2), 468–475 (2006).
33. D.E. Aspnes, "Approximate solution of ellipsometric equations for optically biaxial crystals," J Opt Soc Am **70**(10), 1275–1277 (1980).
34. T. Kimoto and J.A. Cooper, *Fundamentals of Silicon Carbide Technology: Growth, Characterization, Devices and Applications* (John Wiley & Sons, Singapore, 2014).
35. Q. Li, A.Y. Polyakov, M. Skowronski, E.K. Sanchez, M.J. Loboda, M.A. Fanton, T. Bogart, and R.D. Gamble, "Nonuniformities of electrical resistivity in undoped 6H-SiC wafers," J Appl Phys **97**, 113705 (2005).
36. J.Y. Yu, X.L. Yang, Y. Peng, X.F. Chen, X.B. Hu, and X.G. Xu, "Inhomogeneity of Minority Carrier Lifetime in 4H-SiC Substrates," Crystallogr Rep **65**(7), 1231–1236 (2020).
37. L. Zhao and H. Wu, "A correlation study of substrate and epitaxial wafer with 4H-N type silicon carbide," J Cryst Growth **507**, 109–112 (2019).